Clays and Clay Minerals, Vol. 60, No. 6, 561–573, 2012.

CHANGES IN STRUCTURE, MORPHOLOGY, POROSITY, AND SURFACE ACTIVITY OF MESOPOROUS HALLOYSITE NANOTUBES UNDER HEATING

PENG YUAN[1,*], DAOYONG TAN[1,2], FAÏZA ANNABI-BERGAYA[3], WENCHANG YAN[1,2], MINGDE FAN[4], DONG LIU[1], AND HONGPING HE[1]

[1] CAS Key Laboratory of Mineralogy and Metallogeny, Guangzhou Institute of Geochemistry, Chinese Academy of Sciences, Guangzhou 510640, China
[2] Graduate School of the Chinese Academy of Science, Beijing 100049, China
[3] Centre de Recherche sur la Matière Divisée, CNRS-Université d'Orléans, 1b, Rue de La Férollerie, Orléans Cedex 2, France
[4] College of Environment and Resources, Inner Mongolia University, Hohhot 010021, China

Abstract—The objective of the present study was to investigate changes in the structural, textural, and surface properties of tubular halloysite under heating, which are significant in the applications of halloysite as functional materials but have received scant attention in comparison with kaolinite. Samples of a purified halloysite were heated at various temperatures up to 1400ºC, and then characterized by X-ray diffraction, electron microscopy, Fourier-transform infrared spectroscopy, thermal analysis, and nitrogen adsorption. The thermal decomposition of halloysite involved three major steps. During dehydroxylation at 500−900ºC, the silica and alumina originally in the tetrahedral and octahedral sheets, respectively, were increasingly separated, resulting in a loss of long-range order. Nanosized (5−40 nm) γ-Al_2O_3 was formed in the second step at 1000−1100ºC. The third step was the formation of a mullite-like phase from 1200 to 1400ºC and cristobalite at 1400ºC. The rough tubular morphology and the mesoporosity of halloysite remained largely intact as long as the heating temperature was <900ºC. Calcination at 1000ºC led to distortion of the tubular nanoparticles. Calcination at higher temperatures caused further distortion and then destruction of the tubular structure. The formation of hydroxyl groups on the outer surfaces of the tubes during the disconnection and disordering of the original tetrahedral and octahedral sheets was revealed for the first time. These hydroxyl groups were active for grafting modification by an organosilane (γ-aminopropyltriethoxysilane), pointing to some very promising potential uses of halloysite for ceramic materials or as fillers for novel clay-polymer nanocomposites.

Key Words—Group, Metahalloysite, Organosilane Modification, Thermal Transformation, Tubular Halloysite, Structural and Textural Properties.

INTRODUCTION

Halloysite-10 Å ($Al_2(OH)_4Si_2O_5{\cdot}2H_2O$) is a hydrated polymorph of kaolinite with a layer of water molecules between the 1:1 aluminosilicate layers. Nanoscaled tubular halloysite, also known as 'halloysite nanotubes,' is the dominant form of naturally occurring halloysite and results from the wrapping of the clay mineral layers, under favorable geological conditions, to form multi-layer nanotubes. This wrapping is driven by a mismatch between the oxygen-sharing tetrahedral and octahedral sheets in the 1:1 layer (Bates *et al.*, 1950; Singh, 1996). Halloysite occurs commonly in both soils and weathered rocks and is formed by the alteration of a wide variety of types of both igneous and non-igneous rocks. In particular, halloysite often forms a major component of soils derived from volcanic materials in wet tropical and subtropical regions (Joussein *et al.*, 2005). Tubular halloysite has attracted increasing interest in various fields, *e.g.* as a nanoscale reactor (Shchukin *et al.*, 2005), for clay-polymer nanocomposites (Li *et al.*, 2008), and as a support for the entrapment and controlled release of functional guests (Levis and Deasy, 2002; Lvov *et al.*, 2008; Hughes and King, 2010), on account of its unique one-dimensional mesoscopic (2−50 nm) to macroscopic (>50 nm) porous structure and its economic viability (Lvov *et al.*, 2008).

Numerous studies on the calcination of kaolinite have been conducted since Brindley and Nakahira (1959) pioneered the study of the kaolinite-to-mullite reaction sequence. The thermal dehydroxylation and transformation behavior of kaolinite is one of the most thoroughly investigated reactions (Rocha and Klinowski, 1990) because of its importance for ceramic processing. The intermediate states and the equilibrium end point of the kaolinite−mullite reaction have been well defined by various methods including magic-angle spinning nuclear magnetic resonance (MAS NMR) (Brown *et al.*, 1985; MacKenzie *et al.*, 1985; Rocha and Klinowski, 1990; Massiot *et al.*, 1995), transmission electron microscopy (TEM) (Bergaya *et al.*, 1996; Lee *et al.*, 1999), infrared spectroscopy (Percival *et al.*, 1974; Vassallo *et al.*, 1992; Frost and Vassallo, 1996), electron paramagnetic resonance (Djemai *et al.*, 2001), X-ray diffraction (XRD), and thermal analysis (Dion *et al.*, 1998; Kristóf *et al.*, 1998).

* E-mail address of corresponding author:
yuanpeng@gig.ac.cn
DOI: 10.1346/CCMN.2012.0600602

As summarized in the outline by Smith *et al*. (1993), the reaction scheme for the calcination of kaolinite initially involves dehydroxylation between 600 and 850ºC, where most of the OH groups are removed, leading to reduced coordination of originally octahedral aluminum. The metakaolinite formed in this step is X-ray amorphous, but the *ab* order is preserved while some disorder is introduced along the *c* axis (Bergaya *et al.*, 1996). A large exothermic event at ~980ºC, believed to be triggered by removal of the last hydroxyls, is due to the formation of a distinct alumina-rich phase. Further heating to 1400ºC results in the final equilibrium products, namely a 3:2 mullite ($3A1_2O_3 \times 2SiO_2$) and cristobalite.

Much less attention has been paid to the thermal transformation of halloysite. The reaction mechanism under heating (after dehydration) of halloysite had been postulated to be analogous to that of kaolinite because halloysite is structurally and chemically similar to kaolinite. This assumption was supported by Smith *et al.* (1993), but the halloysite sample used in their work contained considerable impurities (quartz and cristobalite), which inevitably affected the interpretation of the spectroscopic characterization and, thus, decreased the reliability of the results obtained.

Halloysite possesses a tubular morphology, in contrast to the plate-like nature of kaolinite. The morphological and textural characteristics (*e.g.* porosity) of the calcined halloysite, accordingly, should be different from those of calcined kaolinite. More importantly, changes to the surface reactivity may be anticipated to result from calcination of halloysite. All of the above-mentioned changes are of significance for applications of halloysite nanotubes as adsorbents, as support materials, and as fillers for novel clay-polymer nanocomposites. However, very few studies on the changes of halloysite under heating have been reported previously (Joussein *et al.*, 2005).

Because of the points above, a very pure tubular halloysite sample was used in the present work, the behavior of which under heating was investigated by thermal analysis, nitrogen adsorption, XRD, Fourier-transform infrared spectroscopy (FTIR), scanning electron microscopy (SEM), and TEM. The key mechanisms of the changes of the surface groups of halloysite and their availability for organosilane modification were also explored.

EXPERIMENTAL

Materials and methods

A high-grade halloysite sample was obtained from Linfen, Shanxi Province, China. The small amount of natroalunite impurity was removed by hand picking followed by repeated sedimentation. The chemical composition of the purified halloysite (denoted as Hal in this paper) as determined from chemical analysis was, in percent by mass of the respective oxide forms: SiO_2, 41.05; Al_2O_3, 34.97; Fe_2O_3, 0.30; MgO, 0.16; CaO, 0.23; Na_2O, 0.25; K_2O, 0.06; MnO, 0.03; and TiO_2, 0.22; and loss on ignition, 22.76.

Portions of Hal were heated in a programmed, temperature-controlled muffle furnace at scheduled temperatures (120−1400ºC) for 1 h. The products were ground into powders using an agate mortar and were denoted as 'Hal-X,' where X was the value, in degrees celsius, of the heating temperature.

The surface reactivity of some calcined halloysite powders was evaluated by organosilane modification. The modification procedure was as follows: 2 mL of γ-aminopropyltriethoxysilane (APTES; 99%, Aldrich) was dissolved in 25 mL of dry toluene (AR grade), and ~0.6 g of Hal powder was added to the APTES-toluene mixture. The dispersion was treated ultrasonically for 0.5 h and then refluxed at 120ºC under constant stirring (400 rpm) for 20 h. The solid phase in the resultant mixture was filtered, washed six times with large amounts of fresh toluene to remove the excess organosilane, and then dried overnight at 90ºC for curing. The APTES-modified calcined halloysite powders were differentiated from the starting powders by postfixing '/M.' For example, Hal-900/M refers to the material that was thermally treated at 900ºC and then modified using ATPES.

Characterization techniques

The XRD patterns were recorded on a Bruker D8 Advance diffractometer (Mannheim, Germany) with Ni filter and CuKα radiation (λ = 0.154 nm) generated at 40 kV and 40 mA. The scan rate was 1º2θ/min.

Fourier-transform infrared absorbance spectra of the heating products of Hal were recorded at room temperature using a Bruker Vertex-70 FTIR spectrometer (Mannheim, Germany). The specimens used for FTIR measurement were prepared by mixing 0.9 mg of sample powder with 80 mg of KBr and pressing the mixture into a pellet. For each measurement, 64 scans were collected at a resolution of 2 cm^{-1}. Diffuse reflectance infrared Fourier-transform (DRIFT) spectra in the hydroxyl region were collected (64 scans at 2 cm^{-1} resolution) on the diffuse reflectance attachment. A portion of the powder was packed lightly into a 4 mm inner-diameter microsample cup for DRIFT spectra collection, and the spectra were normalized against a KBr background reference.

A deuteration experiment was performed as an additional check for the band assignments of the surface hydroxyl groups. Deuterated powders were prepared following the procedure of Koretsky *et al.* (1997). The sample powder was placed in a glass desiccator together with an uncapped vial of D_2O. After three days of D_2O exposure, the powder was removed from the desiccator and used for DRIFT measurement at room temperature. The deuterated halloysite heating products were differentiated from the original heating products by postfixing '/D.'

Thermogravimetric (TG) and differential scanning calorimetry (DSC) analyses were performed using a Netzsch STA 409PC instrument (Selb, Germany). Approximately 10 mg of Hal was heated in a platinum crucible from 30 to 1400ºC at a rate of 5ºC/min under a highly pure N_2 atmosphere (20 cm^3/min).

N_2 adsorption-desorption isotherms were determined with a Micromeritics ASAP2020 system (Norcross, Georgia, USA) at boiling nitrogen temperature. Sample powders were outgassed at 150ºC for 12 h before measurement. The specific surface area of the powder, S_{BET}, was calculated by the multiple-point Brunauer-Emmett-Teller method (Gregg and Sing, 1982), and the total pore volume, V_{pore}, was evaluated from nitrogen uptake at a relative pressure of ~0.97. The Barrett-Joyner-Halenda (BJH) method was used to calculate the pore-size distribution (PSD) curve from the desorption isotherms (Gregg and Sing, 1982).

Observations by TEM were recorded using a 200 kV JEOL JEM-2100 high-resolution transmission electron microscope (Tokyo, Japan). Selected area electron diffraction (SAED) was used for structural characterization, and fast Fourier transform (FFT) of high-resolution TEM (HRTEM) images was used for determination of lattice parameters. Energy dispersive X-ray (EDX) analysis was used for the compositional analysis. The TEM specimens were prepared as follows: the clay or heating product powder was dispersed ultrasonically in ethanol for 5 min, and then a drop of the suspension was deposited onto a carbon-coated copper grid, which was left to stand for 10 min before being transferred into the microscope. The SEM images were obtained using a 5 kV FEI-Sirion 200 field-emission scanning electron microscope (Portland, Oregon, USA).

RESULTS AND DISCUSSION

Structure and phase transformations of halloysite under heating

XRD results. Hal showed a 001 reflection at ~8.85º2θ (Figure 1a), which corresponds to a basal spacing of 0.998 nm and identifies Hal as Halloysite-10 Å. After heating at 120ºC, Hal was converted to Halloysite-7 Å by loss of interlayer water (Joussein *et al.*, 2006), indicated by the 001 diffraction at 0.738 nm (*d* value) of Hal-120 (Figure 1b). The XRD pattern of Hal-400 was like that of Hal-120 (Figure 1c), but the intensities of the halloysite reflections from Hal-500 were markedly less (Figure 1d). The patterns of Hal-600 to Hal-900 showed broad diffraction maxima (Figure 1e–h) owing to dehydroxylation and the formation of an X-ray amorphous product, metahalloysite (Smith *et al.*, 1993).

The XRD pattern of Hal-1000 (Figure 1i) showed a broad reflection centered at ~21.1º2θ (*d* = 0.421 nm) which was attributed to the dissociative amorphous SiO_2 that segregated from the metahalloysite. Moreover, reflections corresponding to *d* values of 0.240 nm, 0.198 nm, and 0.140 nm should be assigned to γ-Al_2O_3, according to the Joint Committee on Powder Diffraction Standards (JCPDS) reference No. 00-010-0425 in the database of the International Centre for Diffraction Data. The γ-Al_2O_3 must be nanocrystalline because the relevant reflections were very broad. Hal-1100 exhibited an XRD pattern (Figure 1j) similar to that of Hal-1000.

After heating at 1200ºC, the reflections assigned to γ-Al_2O_3 were not present but those of mullite were well resolved (Figure 1k). After heating at higher temperatures, the mullite diffractions were more prominent (Figure 1l,m) and particularly the (101) reflection of cristobalite with a *d* value of 0.408 nm was clearly apparent after heating at 1400ºC (Figure 1m).

TG and DSC results. Two clear episodes of rapid mass loss were resolved by thermogravimetric analysis (Figure 2) of Hal. The first, at 50–150ºC, is ascribed

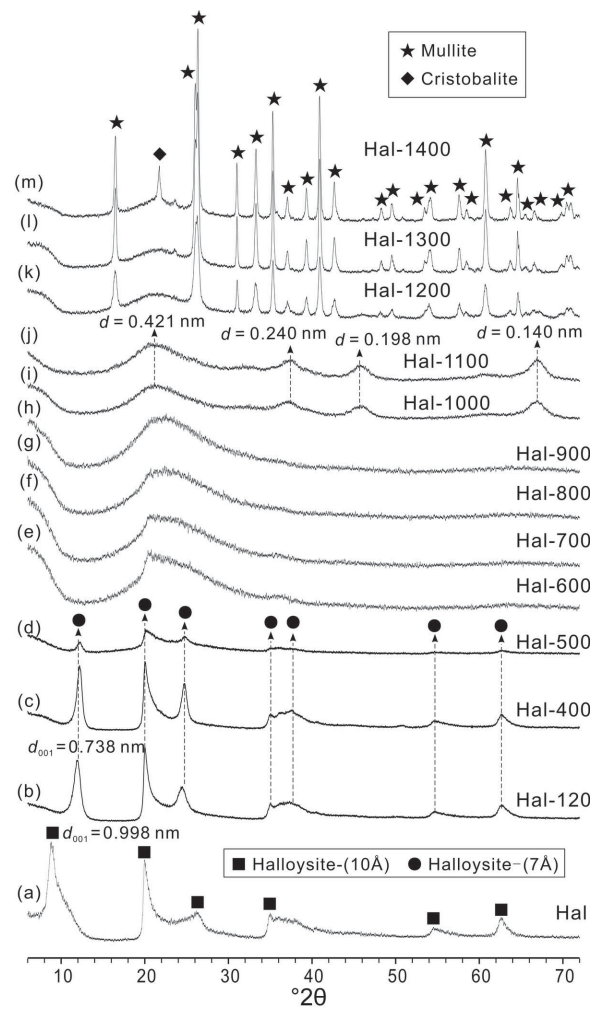

Figure 1. XRD patterns (CuKα) of purified halloysite (Hal) and its heating products.

mainly to dehydration, including removal of the physically adsorbed water and the interlayer water during the transformation from Halloysite-10 Å to Halloysite-7 Å (Joussein *et al.*, 2006). The second, in the 400–550ºC range corresponding to the derivative thermogravimetry (DTG) peak centered at 518ºC, can be attributed to dehydroxylation of Hal. This confirms the suggestion of Frost and Vassallo (1996) that dehydroxylation of halloysite starts at a lower temperature than that of kaolinite. These dehydration and dehydroxylation steps are well correlated to the endothermic peaks at 85 and 519ºC in the corresponding DSC curve (Figure 2).

A narrow exothermic peak at 996ºC corresponds to an exotherm that has been discussed comprehensively for kaolinite in the literature, as described above. Debate has taken place as to whether the alumina-rich phase formed in this event is a spinel-like γ-Al_2O_3 or an alumina-rich mullite (Okada *et al.*, 1986; Brindley and Lemaitre, 1987; Sonuparlak *et al.*, 1987). Based on a comprehensive ^{29}Si and ^{27}Al MAS NMR study, Smith *et al.* (1993) proposed that the exotherm at 996ºC of halloysite should be attributed to the formation of γ-Al_2O_3 on a very fine scale (<5 nm). This proposal is supported by the XRD evidence for nanocrystalline γ-Al_2O_3 in Hal-1000 (Figure 1i). Moreover, the DSC curve of Hal exhibited a minor exotherm not shown in previous studies, starting at ~1240ºC and centered at 1280ºC (Figure 2). This exothermic peak should be attributed to the phase transformation from γ-Al_2O_3 and amorphous SiO_2 to mullite, which, given the rapid heating in the thermal analysis, is consistent with the presence of a substantial amount of mullite in Hal-1200.

FTIR and DRIFT results. The assignment of peaks in the FTIR spectra to vibrational modes in heating products of Hal (Figure 3, Table 1) was based on previous reports on halloysite, alumina, and mullite (Frost and Vassallo, 1996; Morterra and Magnacca, 1996; Koretsky *et al.*, 1997; Madejová and Komadel, 2001; Voll *et al.*, 2001; Joussein *et al.*, 2005). Hal-120 and Hal-400 showed similar spectra (Figure 3a–b), but some differences were obvious in the FTIR spectrum of Hal-500, which was altered substantially by dehydroxylation as revealed by TG and XRD. Absorption at 546 cm^{-1}, the Al–O–Si deformation band, was much less in Hal-500 (Figure 3c), indicating that dehydroxylation was accompanied by destruction of Al–O–Si linkages of halloysite. This absorption peak was even smaller in the spectrum of Hal-600 (Figure 3d) and was absent from that of Hal 700 (Figure 3e), suggesting a phase separation of the amorphous SiO_2 and Al_2O_3 in metahalloysite.

A very weak band at 560 cm^{-1} appeared in the spectra of Hal-1000 and Hal-1100 (Figure 3h and i) which is assigned to the Al–O stretching vibration associated with octahedrally coordinated Al (Al^{VI}) in γ-Al_2O_3 (Voll *et al.*, 2001). The occurrence of this band reflects the formation of nanocrystalline γ-Al_2O_3. A well resolved peak found in the spectra of Hal-1200, Hal-1300, and Hal-1400 at 556 cm^{-1} (Figure 3j–l) is typical of Al^{VI}–O stretching in mullite (Voll *et al.*, 2002).

The Si–O–Si bending band (at 470 cm^{-1} in halloysite) broadened and shifted gradually toward lower wavenumbers as the calcination temperature increased from 500 to 900ºC (Figure 3c–g), a result reflecting progressive disordering of metahalloysite and an increase of the mean bond angle in the Si–O–Si

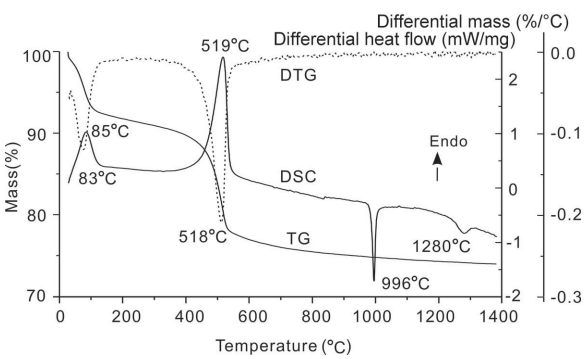

Figure 2. TG, DTG, and DSC curves of Hal.

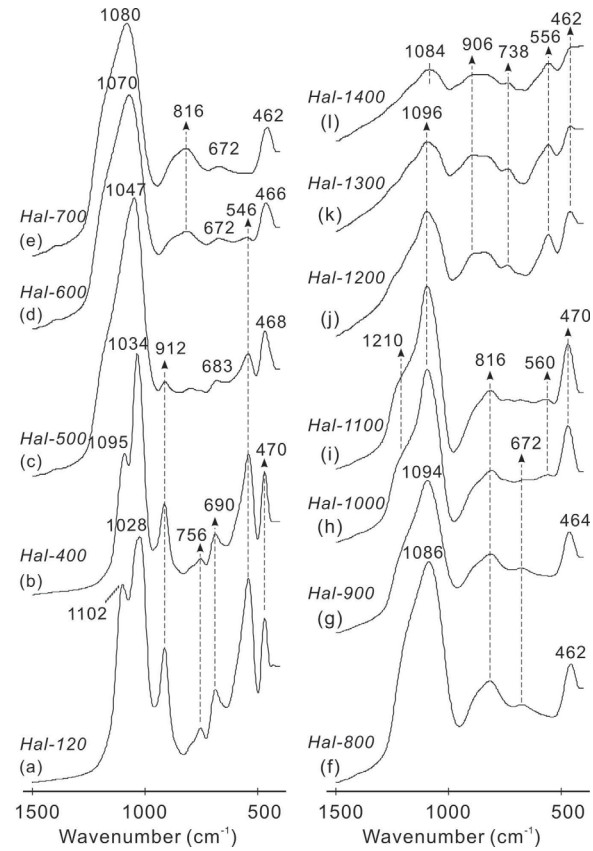

Figure 3. FTIR absorbance spectra of the heating products of purified halloysite (Hal).

Table 1. Positions and assignments of the IR vibration bands.

Position (cm^{-1})	Assignments
3745	O−H stretching of silanols in amorphous silica
3700	O−H stretching of inner-surface hydroxyl groups[a]
3673	O−H stretching of inner-surface hydroxyl groups[b]
3663	O−H stretching of the aluminols in alumina
3626	O−H stretching of inner hydroxyl groups
3250	O−H stretching of water
2933	CH_2 stretching
1102	Perpendicular Si−O stretching
1028−1096	In-plane Si−O−Si stretching
912	Al−O−H deformation of inner hydroxyl groups
906	Al−O vibration associated with four coordinated Al
816	Al−O vibration associated with six coordinated Al
756	Perpendicular Si−O stretching
738	Al−O vibration associated with four coordinated Al
690	Perpendicular Si−O stretching
672	Al−O vibration associated with five coordinated Al
556/560	Al−O stretching vibration associated with six coordinated Al
546	Deformation of Al−O−Si
470	Deformation of Si−O−Si

[a] Vibration with a transition moment nearly perpendicular to the (001) plane.
[b] Vibration with a transition moment lying in the (001) plane (Farmer, 1998).

network. A similar mechanism for calcined kaolinite was proposed by MacKenzie *et al*. (1985) on the basis of ^{29}Si NMR results. In the spectra of Hal-1000 and Hal-1100 (Figure 3h and i), the Si−O−Si stretching band was again at 470 cm^{-1} and should be attributed to amorphous silica (Zhuravlev, 1993). Note that narrowing of the band at 470 cm^{-1} occurred for Hal-1000 and Hal-1100. This reflected the ordering of the Si−O−Si network to some extent. A possible reason for the re-ordering is that some amorphous silica might have been involved in the formation of nanocrystalline mullite or cristobalite at 1000−1100ºC. However, even if these nanocrystalline species existed, they were difficult to observe so that the exact mechanism for the re-ordering of the silica structure remains unclear at this stage. For materials calcined at higher temperatures, the Si−O−Si stretching band occurred at 462 cm^{-1} with a clearly decreased intensity (Figure 3j−l), probably owing to consumption of the amorphous silica during the formation of mullite.

The absorption bands for Si−O vibrations (690 cm^{-1}, 756 cm^{-1}, and 1102 cm^{-1}) exhibited almost identical trends with increasing calcination temperature. Their intensities in metahalloysite (Hal-500 and above) were substantially less than in halloysite with an obvious wavenumber shift (Figure 3d), implying the breaking down of the ordered Si_2O_5 network. The originally separate band at 1102 cm^{-1} could not be resolved from the in-plane Si−O stretching band (initially at 1028 cm^{-1}) in metahalloysite (Figure 3a−g), because the latter band shifted to progressively higher wavenumbers as calcination temperature increased (to ~1094 cm^{-1} for calcination at 900ºC, Figure 3g). This phenomenon reflects progressive disordering of the calcined halloysite with increase of treatment temperature. For Hal-1100 the Si−O stretching band was at 1096 cm^{-1} and had a shoulder at higher wavenumbers (~1210 cm^{-1}), which might have resulted from the presence of amorphous silica (Shoval *et al.*, 2001), supporting the proposal that at this temperature silica was expelled from metahalloysite. For material calcined at the highest temperature, 1400ºC, a broad and asymmetric band centered at ~1084 cm^{-1} was seen. Vibrations of Si−O in several different environments, in both mullite (Voll *et al.*, 2001) and cristobalite (Vassallo *et al.*, 1992; Shoval *et al.*, 1997; Shoval *et al.*, 2001), might have contributed simultaneously to this band.

A broad band at ~816 cm^{-1} became apparent in the spectra of halloysite calcined at 600ºC and above (Figure 3). It is primarily assigned to ^{VI}Al−O stretching. Tetrahedrally coordinated Al (^{IV}Al) in γ-Al_2O_3 may also contribute to this broad band at high temperatures (1000 and 1100ºC) according to Morterra and Magnacca (1996). As the calcination temperature became >1100ºC, two new bands appeared at 906 cm^{-1} and 738 cm^{-1} which were assigned to ^{IV}Al−O stretching in mullite (Voll *et al.*, 2002). Meanwhile, the original 816 cm^{-1} component was weakened slightly upon increasing treatment temperature (Figure 3j−l).

The absorption band at ~672 cm^{-1}, resolved in the spectra of halloysite calcined at 600−900ºC (Figure 3d−g), is assigned to the Al−O vibration involving the five-coordinated Al of metahalloysite. This assignment is based on the proposal that five-coordinated Al exists in disordered metahalloysite

formed in the 600−900ºC temperature range, as revealed by the comprehensive ^{27}Al MAS NMR work of Smith *et al*. (1993). Several high-field NMR studies on some aluminosilicates (Bunker *et al.*, 1991), SiO_2-Al_2O_3 glasses (Sato *et al.*, 1991), and calcined kaolinite (Massiot *et al.*, 1995; He *et al.*, 2004) have actually shown that the occurrence of ^{V}Al is much more common in disordered systems than might be supposed given its rarity in crystalline compounds. This kind of Al coordination is an intermediate during the transformation from $AlO_2(OH)_4$ to AlO_4. In the spectra of Hal-1000 and Hal-1100 (Figure 3h and i), the 672 cm^{-1} band was no longer clearly evident, indicating the disappearance of the intermediate ^{V}Al. This result is in good agreement with ^{27}Al MAS NMR studies of halloysite and kaolinite calcined at high temperatures (Smith *et al.*, 1993; Massiot *et al.*, 1995), in which only two Al signals, attributed to ^{IV}Al and to newly formed ^{VI}Al, were shown.

The hydroxyl groups of halloysite heating products were studied by DRIFT. This technique is more useful than FTIR for detection of the hydroxyl stretching region of silicate minerals (Frost and Johansson, 1998). It works with no interference through sample preparation and is sensitive to the detection of surface groups (Frost and Johansson, 1998; Yuan *et al.*, 2004). The DRIFT spectra of halloysite heating products showed no evident change with increased heating temperature through 400ºC (Figure 4a−c), but after heating at 500ºC the bands due to O−H vibration of both inner-surface hydroxyl groups (at 3700 cm^{-1}) and inner hydroxyl groups (3626 cm^{-1}) were much smaller (Figure 4c). Moreover, a 3673 cm^{-1} band was resolved which should be attributed to vibration of the inner-surface hydroxyl groups (Frost and Johansson, 1998; Farmer, 1998), and was concealed in spectra from lower-temperature products by the 3700 cm^{-1} band, which was broad and asymmetric toward lower wavenumbers. The 912 cm^{-1} band in the FTIR spectrum of Hal-500, due to Al−O−H bending involving inner hydroxyl groups, was also substantially reduced in intensity (Figure 3c).

In the DRIFT spectrum of Hal-600, the hydroxyl group bands were further weakened and a new band at 3745 cm^{-1} was resolved (Figure 4d). This band is assigned to the isolated surface silanols of the amorphous silica expelled from halloysite (Morrow and McFarlan, 1992). For Hal-700, the 3745 cm^{-1} band was more intense (Figure 4e), indicating the continued formation of amorphous silica. The 3663 cm^{-1} band resolved in the spectrum of Hal-700 should be attributed to the remaining aluminols of the amorphous alumina in metahalloysite (Morterra and Magnacca, 1996; Koretsky *et al.*, 1997). These hydroxyl vibration bands were weakened significantly (Figure 4f) at 800ºC owing to loss of hydroxyls by condensation between OH groups. Absorption at 3745 cm^{-1} by silanols was still resolved in the case of Hal-900 but the intensity was sharply decreased (Figure 4g). No 3745 cm^{-1} band was observed in the spectrum of Hal-1100 (not shown), indicating complete dehydroxylation.

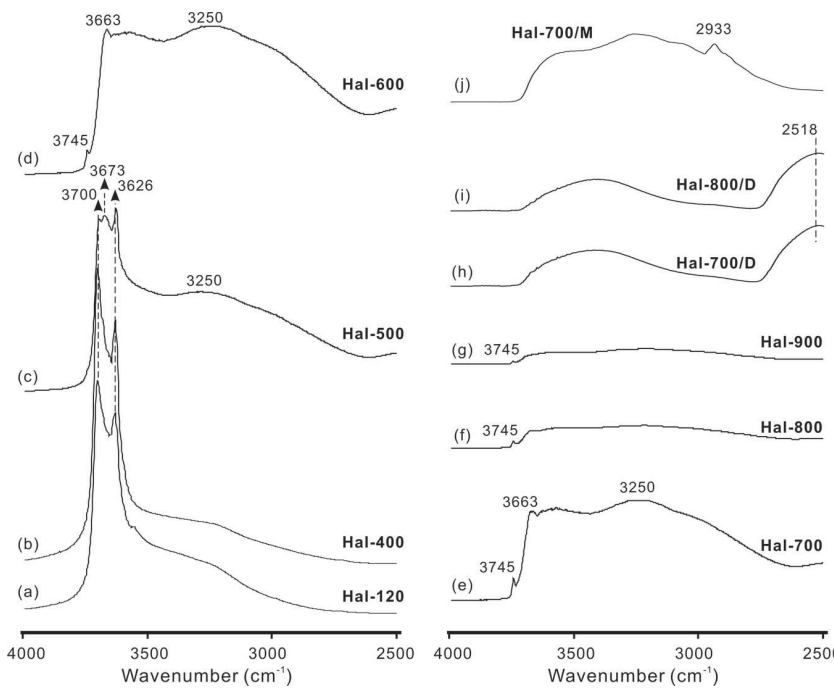

Figure 4. DRIFT spectra (vertical axis: Kubelka-Munk) of Hal heating products (a, b, c, d, e, f, g); deuterated products (h, i); and an APTES-modified product (j).

In the spectra of the deuterated halloysite heating products (Hal-700/D and Hal-800/D), both the 3745 cm^{-1} and 3673 cm^{-1} bands were absent as expected (Figure 4h,i). Instead, a broad band centered at ~2510 cm^{-1} was observed, which results from O–D vibrations in several environments (Drago, 1992), indicating the replacement of the OH groups by OD groups. This result confirms the assignments of the hydroxyl groups in the DRIFT spectra.

Changes in morphology and micro-structure of halloysite nanotubes under heating

The SEM (Figure 5a) and bright-field TEM (Figure 5b) images of Hal showed that the unheated halloysite particles possessed typical cylindrical shapes and contained transparent central areas that run longitudinally along the cylinder (TEM), indicating that the cylinders were hollow and open ended. The SEM images showed that the length of the halloysite nanotubes was ~0.2–1.0 μm, and cross-sectional TEM images showed that the lumen (inner cavity of the nanotube) diameter of the halloysite particles was ~20 nm. The validity of these morphological data is limited by the small number of halloysite particles characterized by microscopic observation.

Heating at ⩽400ºC caused no evident morphological changes to the halloysite particles. Surface mottling, however, was observed in the cases of Hal-600 (inset in Figure 5c), Hal-700, and Hal-800 (no images shown of the latter two). In view of the thermal analysis and XRD results, the mottled appearance was probably caused by the structural disordering associated with dehydroxylation and the phase separation of amorphous SiO_2 and Al_2O_3.

The tubular morphology remained largely intact in the particles of Hal-900 (Figure 5d). Surface mottling, however, was universal, reflecting a high degree of structural disordering. The structural disordering was also revealed by the SAED image (inset in Figure 5d), which shows a broad and isotropic halo, indicating an amorphous structure. This is in good agreement with the XRD results.

Observation of Hal-1000 and Hal-1100 (Figure 6a and b) revealed substantial changes in morphology. Tubular outlines were distorted, unlike those of the original particles. Some nanotubes in Hal-1100 had even become closed, normally at one end and some at both ends (inset in Figure 6b). These phenomena indicated substantial collapse of the tubular structure. Two broad diffraction rings in the SAED pattern (inset in Figure 6a) correspond to the 400 and 440 reflections of γ-Al_2O_3 according to JCPDS reference data (No. 00-010-0425). This result confirms the formation of γ-Al_2O_3 nanoparticles, as already revealed by XRD. Note that no separate γ-Al_2O_3 nanoparticles were observed by TEM in Hal-1100. Instead, nanocrystalline γ-Al_2O_3 was

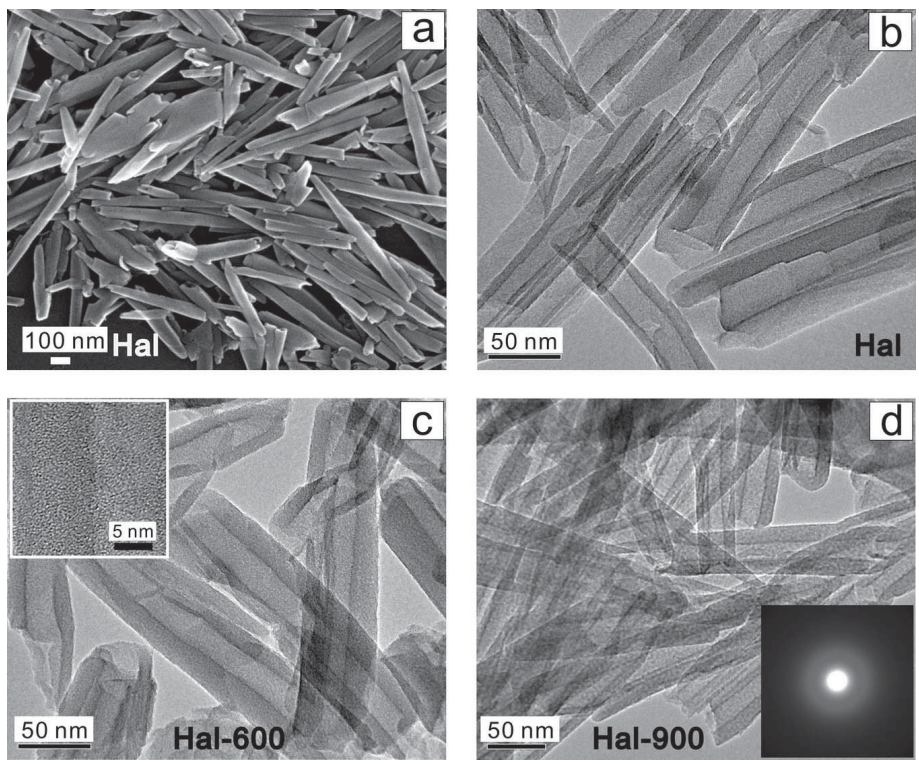

Figure 5. SEM image of Hal (a) and bright-field TEM images of Hal (b), Hal-600 (c), and Hal-900 (d).

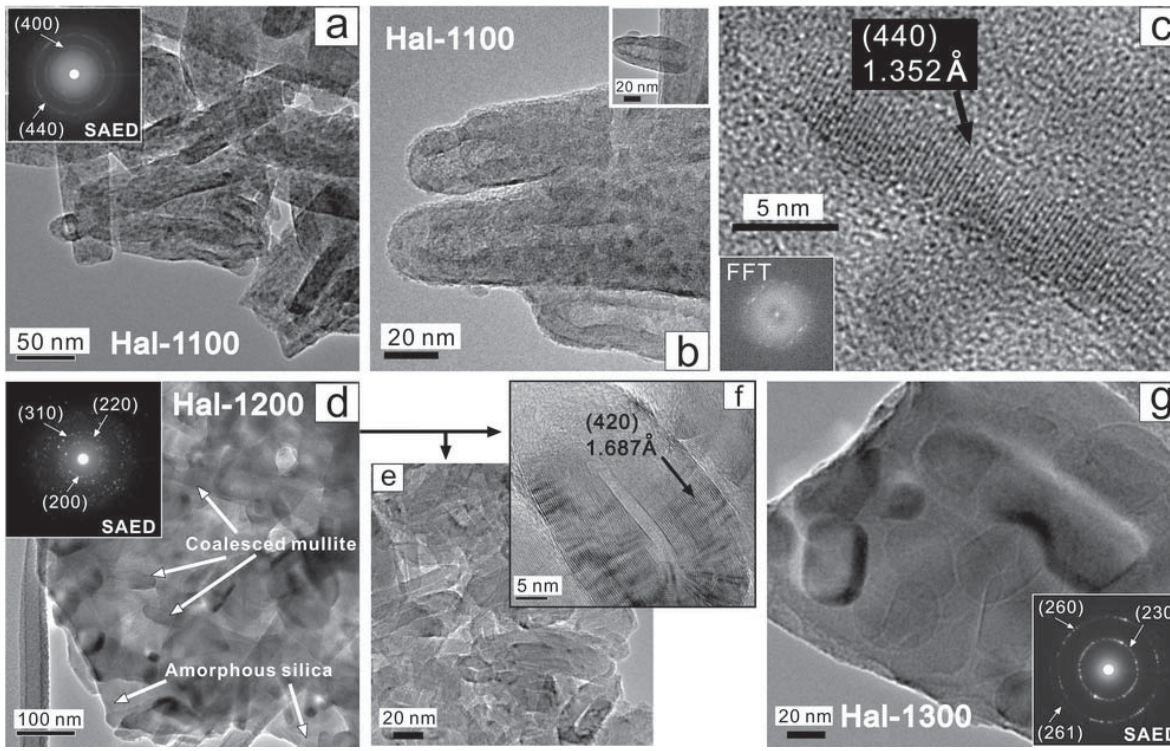

Figure 6. Bright-field TEM images of Hal-1100, -1200, and -1300.

found to have formed locally, *i.e.* within the substrate of the calcined halloysite particles. In particular, crystalline γ-Al_2O_3 domains were observed under HRTEM (Figure 6c; the domain is indicated by an arrow). Based on measurements on the noise-filtered HRTEM image (not shown) derived from FFT processing (the inset in Figure 6c is the FFT pattern), the (440) planes of nanocrystalline γ-Al_2O_3, with interplanar distance of 0.135 nm, were identified.

The width and the length of the nanocrystalline γ-Al_2O_3 domains observed were ~5 nm and 5–15 nm, respectively, as observed in different TEM images. The small size of the nanocrystalline γ-Al_2O_3 particles explains the broad XRD diffractions, and their presence supports the assignment of the 996ºC exotherm to the formation of γ-Al_2O_3.

Calcination at 1200ºC led to large-scale formation of mullite according to XRD. As seen in the TEM image of Hal-1200 (Figure 6d), the mullite nanoparticles in Hal-1200 appear to have coalesced but exhibit rod-like morphology (Figure 6d and e). The mullite nanoparticles seemed to be associated with amorphous SiO_2 substrate (Figure 6d, denoted by arrows) even though the boundaries between the two phases were difficult to identify in TEM. The association of mullite with silica was supported by the SAED image, in which a diffuse halo (corresponding to the amorphous SiO_2) was combined with the diffraction rings of the (200), (220), and (310) reflections of mullite (inset in Figure 6d), which correspond to interplanar distances of 0.360 nm, 0.266 nm, and 0.234 nm, respectively. This result is also in accordance with the corresponding XRD pattern (Figure 1k), which revealed both a broad peak due to amorphous SiO_2 (centered at 21.1º) and the diffraction peaks of mullite. In a high-resolution observation (Figure 6e), the mullite nanoparticles were found to have elliptical shapes, and some possessed hollow structures (Figure 6e and f). An interplanar distance of 0.169 nm corresponding to the (420) planes of mullite was observed (Figure 6f). The nuclei of the mullite phase appeared with preferred orientations relative to the parent nanocrystalline γ-Al_2O_3 to minimize interface energy, and thus grew by interdiffusion of silica and alumina. Considering the scale of Figure 6f, the elliptical form of the mullite particle might have been inherited from a tubular structure like those of Hal-1100, in which ordered γ-Al_2O_3 could react by solid-state reaction with surrounding free amorphous silica at their interface; the small hollow structure (~2 nm × ~20 nm) might be the collapsed lumen of a nanotube in cross section. The large-scale formation of mullite nanoparticles accompanying the aforementioned significant structural transformation, suggests that almost complete destruction of the tubular structure of the halloysite heating products occurred at ~1200ºC.

In the TEM images of Hal-1300 (Figure 6g), the transitional hollow structure of the mullite nanoparticles

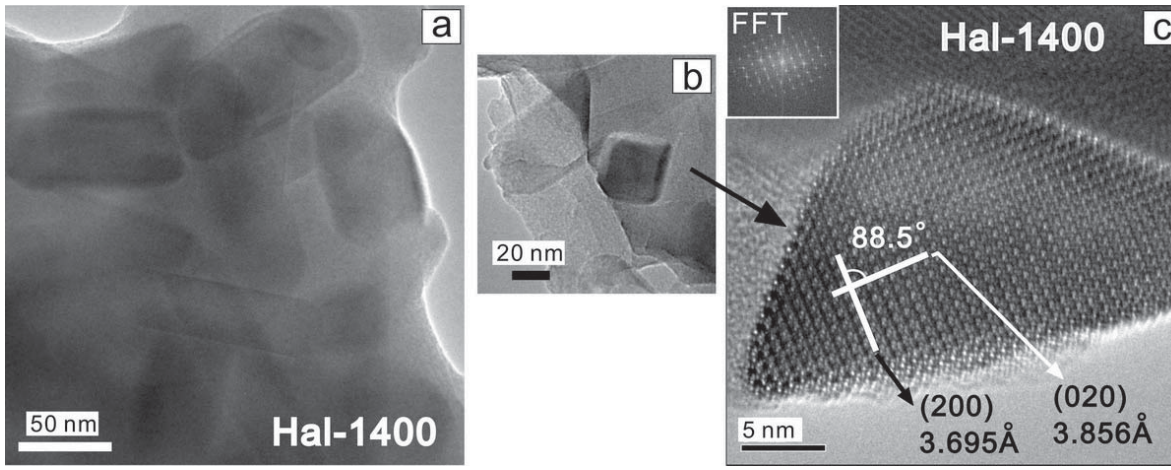

Figure 7. Bright-field TEM images of Hal-1400.

seen in Hal-1200 is not evident. Most mullite particles appear to be non-porous and are ~30−50 nm long. They were confirmed by SAED to be mullite (inset in Figure 6g).

The mullite nanoparticles in Hal-1400 also exhibit rod-like morphologies (Figure 7a), and their average particle size was ~60 nm. Analysis by EDX indicated that the mullite is a final 3:2 mullite resulting from the reaction between the dissociative silica and the previously formed alumina-rich mullite. The TEM characterization (Figure 7c) of a euhedral mullite nanoparticle (Figure 7b) clearly identifies the (200) and (020) planes of mullite and shows that the angle between them is 88.5º, indicating a high crystallinity of mullite at this temperature.

Cristobalite particles were not observed in the TEM images of Hal-1400, although their formation was revealed by XRD (Figure 1m). Cristobalite particles may have been obscured by the overlapped mullite nanoparticles (Figure 7a).

Changes in porosity and specific surface area of halloysite under heating

The nitrogen adsorption-desorption isotherms of halloysite samples (Figure 8a) indicated that all isotherms belong to type IV with H3 hysteresis loops, according to the classification by the International Union of Pure and Applied Chemistry (Gregg and Sing, 1982; Sing and Williams, 2004). The hysteresis loops are associated with the filling and emptying of the mesopores by capillary condensation. The PSD curve of Hal-120 (Figure 8b) shows three primary pore populations, centered at ~3.5 nm, 11 nm, and 22 nm. The 3.5 nm mesopores might be attributed (1) to artificial pores caused by the tensile strength effect interpreted in detail by Groen *et al.* (2003); and (2) to the newly formed mesopores during dehydration of tubular halloysite. The latter assignment is based on the work conducted by Kohyama *et al.* (1978), who found that the rolled layers of tubular halloysite, originally tightly connected to each other, became separated as a result of

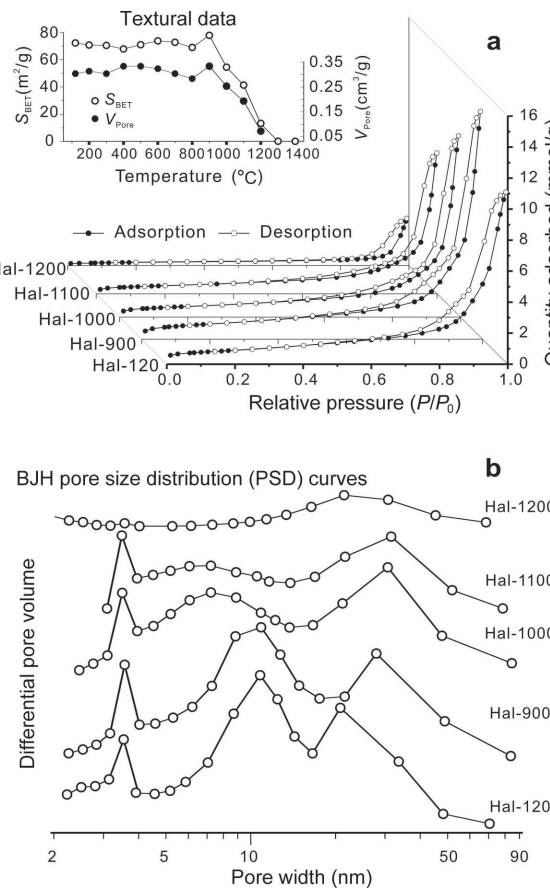

Figure 8. (a) N_2 adsorption-desorption isotherms and textural data (inset) of heating products of Hal. (b) PSD curves of heating products.

dehydration, creating longitudinal pores several nanometers wide. The 11 nm and 22 nm mesopores could be identified readily as the lumens of halloysite. Note that nanotubes with lumen sizes of ~20 nm were observed by TEM (Figure 5), but those of 11 nm were not, probably because of the sampling method used in the TEM characterization. Other mesopores, with diameters ranging from 20 to 40 nm, might represent interparticular porosity between particles in bundles. Clearly the nitrogen adsorption-desorption technique is complementary to TEM imaging, but provides a more complete understanding of porosity because it represents the entire sample.

Hal-400 through Hal-900 exhibited nitrogen adsorption-desorption isotherms and PSD curves similar to those of Hal-120 (Figure 8a,b; results from the intermediate temperatures are not shown). This is in good agreement with the TEM observation that the tubular morphology of halloysite remains largely intact when the heating temperature does not exceed 900ºC. The changes in textural properties from Hal-120 through Hal-800 were small (inset in Figure 8a), suggesting that the porosity of the dehydrated halloysite persisted during heating at temperatures through 800ºC.

Note that the values of specific surface area (78.1 m^2/g) and specific pore volume (0.33 cm^3/g) of Hal-900 were ~10% larger than those of Hal-120 (72.5 m^2/g and 0.30 cm^3/g). This change may have been due to the formation of micropores during surface breakage resulting from structural rearrangement or transformation. Such a mechanism of micropore formation was observed for hierarchically porous carbon materials (Liu *et al.*, 2010). The unexpected high thermal persistence of the tubular structure of halloysite should be meaningful for the design of some novel halloysite-based nanocomposite or ceramic materials.

Calcination of halloysite at 1000ºC and 1100ºC caused obvious decreases in specific surface area and porosity (Figure 8a inset). The reason is that substantial collapse of the tubular structure occurred at these temperatures, as shown by the previously described TEM observation (Figure 6). Hal-1200 showed much smaller values of these textural features (13.2 m^2/g and 0.07 cm^3/g), consistent with the TEM-observed almost complete collapse of the tubular structure at this temperature. The specific surface area values of Hal-1300 and Hal-1400 are very small, the reason being that large mullite particles were formed under sintering.

Availability of the calcined halloysite for surface organosilane modification

The unexpectedly high persistence of the halloysite tubular structure at elevated temperature provides some new insights for designing halloysite-based materials. That the tubular morphology remains intact at temperatures as high as 900ºC is of special significance for designing novel halloysite-based nanocomposite or ceramic materials. For example, a high thermal stability can be postulated for nanosized products of halloysite-metal oxide reactions although they have rarely been investigated (Antill, 2003). Furthermore, the curving and closing of the ends of the tubes may provide a solution for encapsulation of material within guest-loaded halloysite-derived nanotubes for controlled-release purposes, which has been attempted by several methods (Lvov *et al.*, 2008; Yuan *et al.*, 2012).

More important, the DRIFT and TEM characterizations in the present study confirmed the phase separation of SiO_2 and Al_2O_3 upon calcination of halloysite (600−1000ºC), and revealed the character of the related hydroxyl groups for the first time. The work showed that the original siloxane groups at the external surface were replaced, partially or fully, by hydroxyl groups. This change may increase the suitability of halloysite heating products for surface modification, which would be useful for potential applications of organo-modified halloysite heating products for nanocomposites. Little attention has been paid in the literature to modification of the external surface of halloysite nanotubes, although some attempts have been made to modify the interlayer region by intercalation (Tonle *et al.*, 2007), because the siloxane surface is generally regarded as non-reactive. Yuan *et al.* (2008) used γ-aminopropyltriethoxysilane (APTES) for surface modification of unheated halloysite. The hydrolyzed APTES was found to be grafted on to the aluminol groups at the internal surface of the halloysite tubes, but attached to the external siloxane surface primarily by hydrogen bonds. Despite the existence of some external surface defects where aluminol and silanol groups are located and available for modification, the total amount of these defect sites is very small (Yuan *et al.*, 2008).

The availability of the newly formed surface hydroxyl groups of calcined halloysite for organosilane grafting was evaluated by an APTES modification experiment. Hal-700/M exhibited a new 2933 cm^{-1} band in the hydroxyl region (Figure 4j) attributed to the stretching CH_2 vibration. The O−H stretching band of the silanol groups at 3745 cm^{-1} was not apparent in this spectrum, implying that the modification was accompanied by the consumption of surface silanols. Moreover, the aluminol band at 3663 cm^{-1} was weakened substantially, implying that the aluminols that formed during the calcination process were also available for grafting. These results indicated that grafting happened between the surface hydroxyl groups of the calcined halloysite and the hydrolyzed APTES. The specific surface area and specific pore volume of Hal-700/M were 60.5 m^2/g and 0.22 cm^3/g, respectively, smaller than those of Hal-700 (73.0 m^2/g and 0.29 cm^3/g), because the grafted APTES on the surface of Hal decreased the porosity. Similar phenomena were also observed in the cases of Hal-800/M and Hal-900/M (spectra not shown). All of these observations confirmed

the success of the amine modification of the surface of calcined halloysite.

At least two novel applications could be postulated based on the above-mentioned results, including the formation of the surface hydroxyl groups of calcined halloysite and the activity of these groups for organosilane grafting. The first is that the hydroxyl groups which formed, because of their availability for ion-exchange and silylation reaction, could act as new active sites for attracting and fixing functional guests. The second is that organo-modification of the external tube surface of calcined halloysite promises to be a particularly versatile yet site-specific approach to improve the affinity between the calcined halloysite and the polymer substrate in halloysite-polymer nanocomposites. To the authors' knowledge, this last approach has not yet been explored. These potential applications based on external tube surfaces may extend significantly the utility of current lumen-based applications of halloysite.

CONCLUSIONS

Calcination of nanotubular halloysite at temperatures up to 1400ºC resulted in a series of substantial changes in crystalline structure and phase state. Dehydroxylation of halloysite occured from ~500 to ~900ºC, leading to a loss of long-range order and increasing disconnection of the silica and alumina originally in the tetrahedral and octahedral sheets, respectively. The formation of nano-sized (5−15 nm) γ-Al_2O_3, which causes the 996ºC exotherm, occurred under calcination at 1000ºC. Then at 1200ºC and 1300ºC, nanocrystalline mullite was formed with progressively greater silica content. Crystalline 3:2 mullite and cristobalite were formed at ~1400ºC. The mixture of finely divided silica and alumina at 900−1100ºC observed in the present work should be significant in the preparation of novel halloysite-related ceramic materials.

Heating halloysite caused more structural changes than changes in the gross morphology and the porosity at lower temperature. Heating at temperatures up to 900ºC has no obvious influence on the morphology of the particles. The breakdown of the tubular morphology begins at ~1000ºC, when the nanotubes become distorted, and is accompanied by substantial decreases in the porosity as the ends of the tubes close and the tubes collapse at higher temperatures.

Another important change occurring under calcination is the formation of hydroxyl groups at the outer surfaces of the nanotubes during the disconnection and further disordering of silica and alumina originally in the tetrahedral and octahedral sheets: this happens before the breakdown of the tubular structure. The formation of outer-tube surface hydroxyl groups was observed for the first time in the present work, using DRIFT characterization of deuterium-exchanged heating products. These hydroxyl groups are available for organosilane grafting, enabling potential uses for attracting or being loaded with some functional guests in the preparation of halloysite-based functional materials, and for increasing the affinity between calcined halloysite and polymer substrate in clay-polymer nanocomposites.

The present study revealed that heating causes extensive changes in the structure, porosity, and surface reactivity of nanotubular halloysite, offering potential uses for the production of versatile ceramic materials and novel clay-polymer nanocomposites.

ACKNOWLEDGMENTS

Financial support from the Knowledge Innovation Program of the Chinese Academy of Sciences (Grant No. KZCX2-YW-QN101/GIGCAS-IS-1547) and the Natural Scientific Foundation of China (Grant No. 41072032) is gratefully acknowledged. The authors are grateful to Prof. Aihua Yuan and Mr Kangmin Chen for their assistance with TEM characterization.

REFERENCES

Antill, S.J. (2003) Halloysite: A low-cost alternative nanotube. *Australian Journal of Chemistry*, **56**, 723−723.

Bates, T.F., Hildebrand, F.A., and Swineford, A. (1950) Morphology and structure of endellite and halloysite. *American Mineralogist*, **35**, 463−484.

Bergaya, F., Dion, P., Alcover, J.-F., Clinard, C., and Tchoubar, D. (1996) TEM study of kaolinite thermal decomposition by controlled-rate thermal analysis. *Journal of Materials Science*, **31**, 5069−5075.

Brindley, G.W. and Lemaitre, J. (1987) Thermal, oxidation and reduction reactions of clay minerals. Pp. 319−364 in: *Chemistry of Clays and Clay Minerals* (A.C.D. Newman, editor). Longman Scientific & Technical, Harlow, Essex, UK.

Brindley, G.W. and Nakahira, M. (1959) The kaolinite-mullite reaction series: I. A survey of outstanding problems. *Journal of the American Ceramic Society*, **42**, 311−314.

Brown, I.W.M., MacKenzie, K.J.D., Bowden, M.E., and Meinhold, R.H. (1985) Outstanding problems in the kaolinite-mullite reaction sequence investigated by ^{29}Si and ^{27}Al solid-state nuclear magnetic resonance: II. High-temperature transformations of metakaolinite. *Journal of the American Ceramic Society*, **68**, 298−301.

Bunker, B.C., Kirkpatrick, R.J., Brow, R.K., Turner, G.L., and Nelson, C. (1991) Local structure of alkaline-earth boroaluminate crystals and glasses: II. ^{11}B and ^{27}Al MAS NMR spectroscopy of alkaline-earth boroaluminate glasses. *Journal of the American Ceramic Society*, **74**, 1430−1438.

Dion, P., Alcover, J.-F., Bergaya, F., Ortega, A., Llewellyn, P.L., and Rouquerol, F. (1998) Kinetic study by controlled-transformation rate thermal analysis of the dehydroxylation of kaolinite. *Clay Minerals*, **33**, 269−276.

Djemai, A., Balan, E., Morin, G., Hernandez, G., Labbe, J.C., and Muller, J.P. (2001) Behavior of paramagnetic iron during the thermal transformations of kaolinite. *Journal of the American Ceramic Society*, **84**, 1017−1024.

Drago, R.S. (1992) *Physical Methods for Chemists*, 2nd edition. Saunders College Publishing, Mexico.

Farmer, V.C. (1998) Differing effects of particle size and shape in the infrared and Raman spectra of kaolinite. *Clay Minerals*, **33**, 601−604.

Frost, R.L. and Johansson, U. (1998) Combination bands in the infrared spectroscopy of kaolins − a DRIFT spectroscopic study. *Clays and Clay Minerals*, **46**, 466−477.

Frost, R.L. and Vassallo, A.M. (1996) The dehydroxylation of the kaolinite clay minerals using infrared emission spectroscopy. *Clays and Clay Minerals*, **44**, 635–651.

Groen, J.C., Peffer, L.A.A., and Pérez-Ramírez, J. (2003) Pore size determination in modified micro- and mesoporous materials. Pitfalls and limitations in gas adsorption data analysis. *Microporous and Mesoporous Materials*, **60**, 1–17.

Gregg, S.J. and Sing, K.S.W. (1982) *Adsorption, Surface Area and Porosity*, 2nd edition. Academic Press, London.

He, H.P., Guo, J.G., Zhu, J.X., Yuan, P., and Hu, C. (2004) Si-29 and Al-27 MAS NMR spectra of mullites from different kaolinites. *Spectrochimica Acta Part A – Molecular and Biomolecular Spectroscopy*, **60**, 1061–1064.

Hughes, A.D. and King, M.R. (2010) Use of naturally occurring halloysite nanotubes for enhanced capture of flowing cells. *Langmuir*, **26**, 12155–12164.

Joussein, E., Petit, S., Churchman, J., Theng, B., Righi, D., and Delvaux, B. (2005) Halloysite clay minerals – a review. *Clay Minerals*, **40**, 383–426.

Joussein, E., Petit, S., Fialips, C.-I., Vieillard, P., and Righi, D. (2006) Differences in the dehydration-rehydration behavior of halloysites: New evidence and interpretations. *Clays and Clay Minerals*, **54**, 473–484.

Kohyama, N., Fukushima, K., and Fukami, A. (1978) Observation of the hydrated form of tubular halloysite by an electron microscope equipped with an environmental cell. *Clays and Clay Minerals*, **26**, 25–40.

Koretsky, C.M., Sverjensky, D.A., Salisbury, J.W., and D'Aria, D.M. (1997) Detection of surface hydroxyl species on quartz, γ-alumina, and feldspars using diffuse reflectance infrared spectroscopy. *Geochimica et Cosmochimica Acta*, **61**, 2193–2210.

Kristóf, J., Frost, R.L., Horváth, E., Kocsis, L., and Inczéy, J. (1998) Thermoanalytical investigations on intercalated kaolinites. *Journal of Thermal Analysis and Calorimetry*, **53**, 467–475.

Lee, S., Kim, Y.J., and Moon, H.-S. (1999) Phase transformation sequence from kaolinite to mullite investigated by an energy-filtering transmission electron microscope. *Journal of the American Ceramic Society*, **82**, 2841–2848.

Levis, S.R. and Deasy, P.B. (2002) Characterisation of halloysite for use as a microtubular drug delivery system. *International Journal of Pharmaceutics*, **243**, 125–134.

Li, C.P., Liu, J.G., Qu, X.Z., Guo, B.C., and Yang, Z.Z. (2008) Polymer-modified halloysite composite nanotubes. *Journal of Applied Polymer Science*, **110**, 3638–3646.

Liu, D., Yuan, P., Tan, D.Y., Liu, H.M., Fan, M.D., Yuan, A.H., Zhu, J.X., and He, H.P. (2010) Effects of inherent/enhanced solid acidity and morphology of diatomite templates on the synthesis and porosity of hierarchically porous carbon. *Langmuir*, **26**, 18624–18627.

Lvov, Y.M., Shchukin, D.G., Mohwald, H., and Price, R.R. (2008) Halloysite clay nanotubes for controlled release of protective agents. *ACS Nano*, **2**, 814–820.

MacKenzie, K.J.D., Brown, I.W.M., Meinhold, R.H., and Bowden, M.E. (1985) Outstanding problems in the kaolinite-mullite reaction sequence investigated by ^{29}Si and ^{27}Al solid-state nuclear magnetic-resonance: I. Metakaolinite. *Journal of the American Ceramic Society*, **68**, 293–297.

Madejová, J. and Komadel, P. (2001) Baseline studies of the Clay Minerals Society source clays: Infrared methods. *Clays and Clay Minerals*, **49**, 410–432.

Massiot, D., Dion, P., Alcover, J.F., and Bergaya, F. (1995) ^{27}Al and ^{29}Si MAS NMR study of kaolinite thermal decomposition by controlled rate thermal analysis. *Journal of the American Ceramic Society*, **78**, 2940–2944.

Morrow, B.A. and McFarlan, A.J. (1992) Surface vibrational modes of silanol groups on silica. *Journal of Physical Chemistry*, **96**, 1395–1400.

Morterra, C. and Magnacca, G. (1996) A case study: Surface chemistry and surface structure of catalytic aluminas, as studied by vibrational spectroscopy of adsorbed species. *Catalysis Today*, **27**, 497–532.

Okada, K., Otsuka, N., and Ossaka, J. (1986) Characterization of spinel phase formed in the kaolin-mullite thermal sequence. *Journal of the American Ceramic Society*, **69**, C-251–C-253.

Percival, H.J., Duncan, J.F., and Foster, P.K. (1974) Interpretation of the kaolinite-mullite reaction sequence from infrared absorption spectra. *Journal of the American Ceramic Society*, **57**, 57–61.

Rocha, J. and Klinowski, J. (1990) ^{29}Si and ^{27}Al magic-angle-spinning NMR studies of the thermal transformation of kaolinite. *Physics and Chemistry of Minerals*, **17**, 179–186.

Sato, R.K., Mcmillan, P.F., Dennison, P., and Dupree, R. (1991) High-resolution Al-27 and Si-29 MAS NMR investigation of SiO_2-Al_2O_3 glasses. *Journal of Physical Chemistry*, **95**, 4483–4489.

Shchukin, D.G., Sukhorukov, G.B., Price, R.R., and Lvov, Y.M. (2005) Halloysite nanotubes as biomimetic nanoreactors. *Small*, **1**, 510–513.

Shoval, S., Champagnon, B., and Panczer, G. (1997) The quartz-cristobalite transformation in heated chert rock composed of micro and crypto-quartz by micro-Raman and FT-IR spectroscopy methods. *Journal of Thermal Analysis*, **50**, 203–213.

Shoval, S., Boudeulle, M., Yariv, S., Lapides, I., and Panczer, G. (2001) Micro-Raman and FT-IR spectroscopy study of the thermal transformations of St. Claire dickite. *Optical Materials*, **16**, 319–327.

Sing, K.S.W. and Williams, R.T. (2004) Review: The use of molecular probes for the characterization of nanoporous adsorbents. *Particle & Particle Systems Characterization*, **21**, 71–79.

Singh, B. (1996) Why does halloysite roll? – A new model. *Clays and Clay Minerals*, **44**, 191–196.

Smith, M.E., Neal, G., Trigg, M.B., and Drennan, J. (1993) Structural characterization of the thermal transformation of halloysite by solid-state NMR. *Applied Magnetic Resonance*, **4**, 157–170.

Sonuparlak, B., Sarikaya, M., and Aksay, I.A. (1987) Spinel phase formation during the 980ºC exothermic reaction in the kaolinite-to-mullite reaction series. *Journal of the American Ceramic Society*, **70**, 837–842.

Tonle, I.K., Diaco, T., Ngameni, E., and Detellier, C. (2007) Nanohybrid kaolinite-based materials obtained from the interlayer grafting of 3-aminopropyltriethoxysilane and their potential use as electrochemical sensors. *Chemistry of Materials*, **19**, 6629–6636.

Vassallo, A.M., Coleclarke, P.A., Pang, L.S.K., and Palmisano, A.J. (1992) Infrared-emission spectroscopy of coal minerals and their thermal transformations. *Applied Spectroscopy*, **46**, 73–78.

Voll, D., Lengauer, C., Beran, A., and Schneider, H. (2001) Infrared band assignment and structural refinement of Al-Si, Al-Ge, and Ga-Ge mullites. *European Journal of Mineralogy*, **13**, 591–604.

Voll, D., Angerer, P., Beran, A., and Schneider, H. (2002) A new assignment of IR vibrational modes in mullite. *Vibrational Spectroscopy*, **30**, 237–243.

Yuan, P., Wu, D.Q., He, H.P., and Lin, Z.Y. (2004) The hydroxyl species and acid sites on diatomite surface: A combined IR and Raman study. *Applied Surface Science*, **227**, 30–39.

Yuan, P., Southon, P.D., Liu, Z., Green, M.E.R., Hook, J.M., Antill, S.J., and Kepert, C.J. (2008) Functionalization of halloysite clay nanotubes by grafting with γ-aminopropyl-

triethoxysilane. *Journal of Physical Chemistry C*, **112**, 15742–15751.

Yuan, P., Southon, P.D., Liu, Z., and Kepert, C.J. (2012) Organosilane functionalization of halloysite nanotubes for enhanced loading and controlled release. *Nanotechnology*, **23**, 375705.

Zhuravlev, L.T. (1993) Surface characterization of amorphous silica – a review of work from the former USSR. *Colloids and Surfaces A – Physicochemical and Engineering Aspects*, **74**, 71–90.

(*Received 15 May 2012; revised 18 October 2012; Ms. 672; AE: J.M. Wampler*)